Available online at www.sciencedirect.com
ScienceDirect
Journal of Power Sources 168 (2007) 79–89
JOURNAL OF POWER SOURCES
www.elsevier.com/locate/jpowsour

Lead–samarium alloys for positive grids of valve-regulated lead–acid batteries

H.Y. Chen [a,*], S. Li [a], A.J. Li [a], D. Shu [a], W.S. Li [a], C.L. Dou [b], Q. Wang [b], G.M. Xiao [b], S.G. Peng [b], S. Chen [b], W. Zhang [b], H. Wang [b]

[a] *School of Chemistry and Environment, South China Normal University, Guangzhou Guangdong 510631, China*
[b] *Zhuzhou Smelter Group Co., Ltd., Zhuzhou Hunan 412004, China*

Received 26 September 2006; accepted 30 November 2006
Available online 16 December 2006

Abstract

The influence of the rare earth metal, samarium, as an alloying additive on the electrochemical behaviour of pure lead is studied by means of X-ray diffraction, self-depassivation, linear sweep voltammetry and a.c. impedance spectroscopy in 4.87 M H_2SO_4 at 25 °C. Studies on Pb–Sm alloys (Sm = 0.02, 0.04, and 0.12 wt.%) indicate that the oxide film formed on the alloy surface at 0.9 V is thicker than that on pure lead when the alloy contained less than 0.1 wt.% Sm. In addition, samarium exercises little influence on the conversion of $PbSO_4$ to PbO_2 in the oxide film during charging. The electrochemical impedance of the oxide film is much larger than that of the oxide formed on pure lead. With the addition of more than 0.1% Sm, however, the oxide film on the alloy surface is thinner and samarium obviously promotes the conversion of passive $PbSO_4$ in oxide film to conductive PbO_2. The a.c. impedance data show that a high content of samarium greatly inhibits the growth of the passivation layer and decreases the electrochemical impedance of the film.

Keywords: Valve-regulated lead–acid battery; Grid alloy; Lead; Samarium; Electric bicycle; Oxide film

1. Introduction

Two main types of positive grid are widely used in lead–acid batteries [1–4]: one is the low-antimony grid, the other is the lead–calcium grid. Tin [2,5,6] and arsenic, as well as cadmium, have been doped into low-antimony grids to eliminate or suppress the 'antimony effect', i.e., the dissolution and subsequent transfer to the negative electrode with subsequent enhancement of hydrogen evolution. Arsenic is of low density, however, and has a propensity to be oxidized into a virulent oxide. By contrast, calcium is only added to enhance the mechanical properties of the lead alloys [7] and has no influence on their electrochemical behaviour [8]. The hydrogen overpotential at a lead–calcium alloy is much higher (i.e., 200 mV) than that at a common lead–antimony alloy and hence calcium alloys have been manufactured on a large scale.

As an additive, rare earth metals bring advantages to the mechanical properties, corrosion resistance and the conductivity of grids used in lead–acid batteries. During the past few years, several authors have studied lead–calcium and lead–antimony alloys that both contain rare earth metals. Wei et al. [9] tested found that cerium and yttrium can improve the overpotentials of hydrogen and oxygen evolution on Pb–Ca and Pb–Sb alloys and can restrain the reduction of PbO_2 in the corrosion film during the discharge. Recent experiments [10–15] have suggested that the addition of Sm, Ce and Y increases the porosity of the anodic film, which may cause an increase in the ionic conductance produced by the interstitial liquid among the PbO particles in the film and there by lead to a decrease in the resistance of the anodic film.

It is, therefore, our objective to study a new lead–samarium binary alloy as a positive grid for valve-regulated lead acid (VRLA) batteries to replace Pb–Sb–Cd alloys or overcome the shortcomings of conventional Pb–Ca–Sn–Al alloys. Success would reduce the environmental pollution caused by the wide application of Pb–Sb–Cd alloys in VRLA batteries used for electric bicycles in China. Another important aim is to promote the

* Corresponding author. Tel.: +86 20 39310183; fax: +86 20 39310183.
E-mail address: battery@scnu.edu.cn (H.Y. Chen).

0378-7753/$ – see front matter © 2007 Elsevier B.V. All rights reserved.
doi:10.1016/j.jpowsour.2006.11.091

deep-cycle performance of VRLA batteries during service in electric vehicles.

2. Experimental

Lead–samarium binary alloys (with 0.02, 0.04 and 0.12 wt.%) and Pb–Ca–Sn–Al–Sm alloys were processed in the laboratory by melting weighed mixtures of pure lead and pure samarium. Lead alloy rods with 0.3 cm^2 of geometric area were used as working electrodes. Table 1 lists the elemental compositions of the Pb–Ca–Sn–Al–Sm alloys.

Electrochemical tests were performed in a three-electrode cell that was connected to an Autolab PGSTAT-30 potentionstat/galvanostat (ECO Echemie B.V., Holland) supplied with a computer. The reference electrode was a K_2SO_4-saturated mercurous sulfate electrode (E = +0.658 versus SHE) and all working electrode potentials are reported with respect to this reference electrode. The electrolyte was 4.87 M sulfuric acid solution, which was prepared from analytical grade reagent and maintained at 25 °C.

The working electrodes were mechanically polished with successively finer grades of SiC emery paper up to 1500, then with colloidal silica dispersed in water. Samples were finally rinsed with distilled water, then with ethanol, and finally dried. Prior to each experiment and immediately after sample immersion, the polished lead electrode was reduced at −1.2 V to eliminate oxides on the electrode surface.

Electrochemical tests were performed after 1 h potentiostatic oxidation runs at several voltages, namely, 0.5, 0.9, 1.1 and 1.3 V. Each voltage corresponds to conditions that simulate different charge stages of lead–acid batteries.

Self-depassivation measurements were carried out after the electrodes had been maintained at 0.9, 1.1 or 1.3 V for 1 h and the polarization potential cut-off for 5 h.

The metal phases present were identified by X-ray diffraction, XRD analysis over a scan range of 20–80° at a rate: of 0.015° per 0.4 s.

The amplitude of the a.c. signal in the electrochemical impedance spectroscopy (EIS) experiment was 5 mV. The frequency was in the range of 10×10^5 to 10 Hz. The spectra were analyzed using FRA impedance modelling software.

Linear sweep voltammetry (LSV) was performed after the working electrode was polarized at 0.5, 0.9 or 1.3 V for 1 h. The potential was swept from the corresponding polarization voltage to −1.2 V at a rate of 1 mV s^{-1}.

Table 1
Elemental compositions (wt.%) of Pb–Ca–Sn–Al–Sm alloys

	Ca	Sn	Al	Sm
1#	0.05	0.6	0.005	0
2#	0.05	0.6	0.005	0.01
3#	0.05	0.6	0.005	0.1
4#	0.05	0.6	0.005	0.15
5#	0.05	0.6	0.005	0.2
6#	0.05	0.6	0.005	0.25
7#	0.085	0.6	0.005	0.15

The cycle-life of electric-bicycle batteries was tested according to the Chinese machine industry standard 'VRLA Batteries Used for Electric Moped (JB/T10262-2001)'. After being charged at a constant potential of 16 V and with a limited current of 1.5 A for 5.6 h, the battery was discharged with a constant current of 5 A for 1.4 h. When the battery voltage was less than 9.6 V for three times after discharging for 1.4 h, it was considered to have failed and the cycle was terminated. This condition represents 70% DoD at the 2-h rate. Three types of alloy, e.g., Pb–1.5%Sb–1.5%Cd alloy, Pb–0.08%Ca–0.6%Sn–0.02%Al alloy and Pb–0.085%Ca–0.6%Sn–0.005%Al–0.15%Sm alloy, were used as the positive grids for 12-V/10-Ah (2-h rate) VRLA batteries. The negative grids were all of same material, namely, Pb–Ca–Sn–Al alloy.

3. Results and discussion

3.1. Pb–Sm binary alloy

3.1.1. XRD patterns of lead and lead–samarium binary alloys

The XRD patterns of lead and lead–samarium binary alloys are presented in Fig. 1. The results feature a characteristic peak of lead and there is no indication of the presence of other crystal phases.

The following relation exists among the interplanar spacing d, the indices of the crystallographic planes H, K, L and the lattice parameter.

$$\frac{1}{d^2} = \frac{1}{v^2}[H^2b^2c^2\ \sin^2\alpha + K^2a^2c^2\ \sin^2\beta + L^2a^2b^2\ \sin^2\gamma + 2HKabc^2(\cos\alpha\ \cos\beta - \cos\gamma) + 2KLa^2bc(\cos\beta\ \cos\gamma - \cos\alpha) + HLab^2c(\cos\alpha\ \cos\gamma - \cos\beta)] \quad (1)$$

Where:

$$v = abc(1+2\ \cos\alpha\ \cos\beta\ \cos\gamma - \cos^2\alpha - \cos^2\beta - \cos^2\gamma)^{1/2}$$

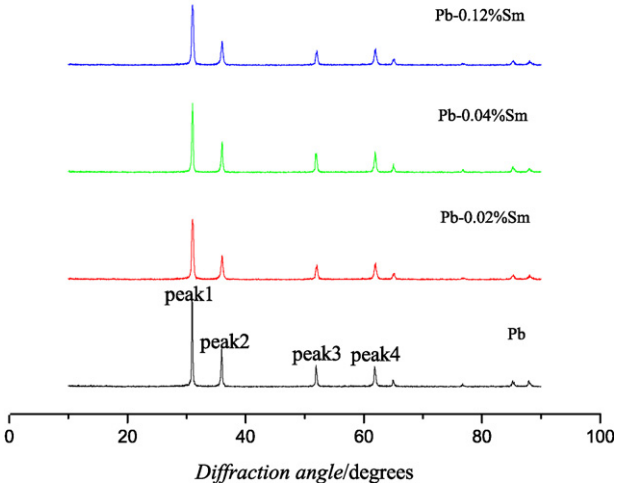

Fig. 1. XRD patterns of lead and lead–samarium binary alloys.

Table 2
Parameters in main diffraction peaks in XRD patterns of lead and lead–samarium binary alloys

	d1 (*HKL*)	d2 (*HKL*)	d3 (*HKL*)
Pb	2.8901 (1 1 1)	2.498 (2 0 0)	1.7604 (2 2 0)
Pb–0.02%Sm	2.8819 (1 1 1)	2.4899 (2 0 0)	1.4969 (3 1 1)
Pb–0.04%Sm	2.8819 (1 1 1)	2.4919 (2 0 0)	1.4989 (3 1 1)
Pb–0.12%Sm	2.8819 (1 1 1)	2.4899 (2 0 0)	1.4969 (3 1 1)

For a cubic system, Eq. (1) should read:

$$\frac{1}{d^2} = \frac{H^2 + K^2 + L^2}{a^2} \quad (2)$$

The cell parameters of four samples were calculated on the basis of Eq. (2) and of the parameters listed in Table 2. The results are as follows: a1 = 4.994 nm, a2 = 4.965 nm, a3 = 4.982 nm, a4 = 4.979 nm. The cell parameters of the lead–samarium alloys are slightly less than those of lead, which indicates that finer grains are obtained.

The atomic radius of lead is 0.175 nm and that of samarium is 0.18 nm. The difference between the two elements is less than 14–15%. Furthermore, the electronegativity of lead is 1.5 while that of samarium is 1.3. The difference, $\Delta x < 0.4$–0.5, indicates that a solid solution over a wide range may be formed.

3.1.2. Open-circuit potential

The self-depassivation of Pb and of Pb–Sm alloy after potentiostatic anodization at 0.9 or 1.1 V for 1 h is shown in Figs. 2 and 3, respectively. The behaviour of the Pb and Pb–0.12%Sm electrodes are similar; the curves remain at the equilibrium potential of PbO·PbSO$_4$/Pb, when the electrodes are anodized in the range of 0.9–1.1 V. The self-depassivation of Pb–0.02%Sm and Pb–0.04%Sm is similar, but the curves lie at the equilibrium potential of PbO/Pb.

The four electrodes were depassivated for 5 h after overcharging at 1.3 V for 1 h (see Fig. 4). Short PbO$_2$/PbSO$_4$ plateaux first appear at 1.1 V, and that for the Pb–0.12%Sm electrode

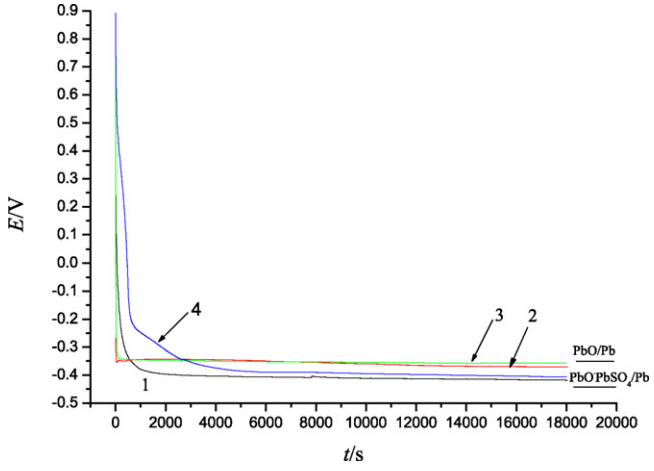

Fig. 2. Self-depassivation of Pb (1) and Pb–Sm alloys (2: Pb–0.02%Sm, 3: Pb–0.04%Sm, 4:Pb–0.12%Sm) after potentiostatic anodization at 0.9 V (vs. Hg/Hg$_2$SO$_4$) for 1 h in 4.87 M H$_2$SO$_4$.

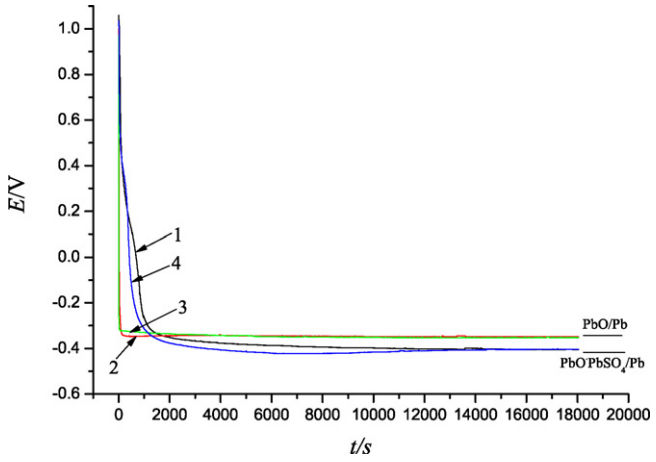

Fig. 3. Self-depassivation of Pb (1) and Pb–Sm alloys (2: Pb–0.02%Sm, 3: Pb–0.04%Sm, 4: Pb–0.12%Sm) after potentiostatic anodization at 1.1 V (vs. Hg/Hg$_2$SO$_4$) for 1 h in 4.87 M H$_2$SO$_4$.

is the longest. This indicates that a more conductive PbO$_2$ is formed during corrosion of the Pb–0.12%Sm electrode. After the plateaux, the self-depassivation curves of the Pb–Sm alloy electrodes polarized at 1.3 V are similar to those for polarization at 0.9 or 1.1 V, but the self-depassivation curve of the Pb electrode arrives at the equilibrium potential of PbSO$_4$/Pb. Typical voltage–time curves on open-circuit were reported in [16,17]. More PbSO$_4$ was formed during corrosion of the Pb electrode, while more PbO and less PbSO$_4$ were produced on the Pb–Sm electrode.

3.1.3. EIS study on PbO growth

When the potential of the anodic oxidation of lead in sulfuric acid solution is in the PbO potential region (−0.40 to 0.95 V), an anodic film with a complex composition will be obtained, i.e., Pb/PbO/3PbO/PbSO$_4$·H$_2$O/PbO·PbSO$_4$/PbSO$_4$, with PbO, PbO·PbSO$_4$ and PbSO$_4$ as the major components.

Electrochemical impedance measurements were carried out after every 1 h of oxidation at a fixed potential value of 0.9 V, on a Pb electrode (1), and on a Pb–Sm electrode (2: Pb–0.02%Sm,

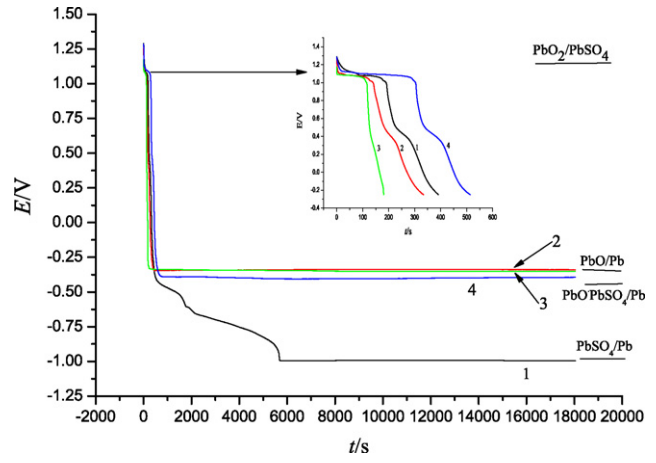

Fig. 4. Self-depassivation of Pb (1) and Pb–Sm alloys (2: Pb–0.02%Sm, 3: Pb–0.04%Sm, 4: Pb–0.12%Sm) after potentiostatic anodization at 1.3 V (vs. Hg/Hg$_2$SO$_4$) for 1 h in 4.87 M H$_2$SO$_4$.

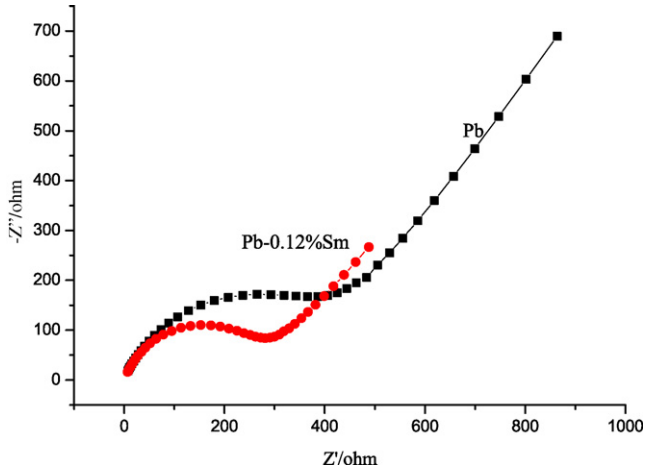

Fig. 5. Nyquist plot of impedance data of Pb electrode and Pb–0.12%Sm electrode, polarized at 0.9 V in 4.87 M H_2SO_4 for 1 h, frequency range from 10^5 to 10 Hz.

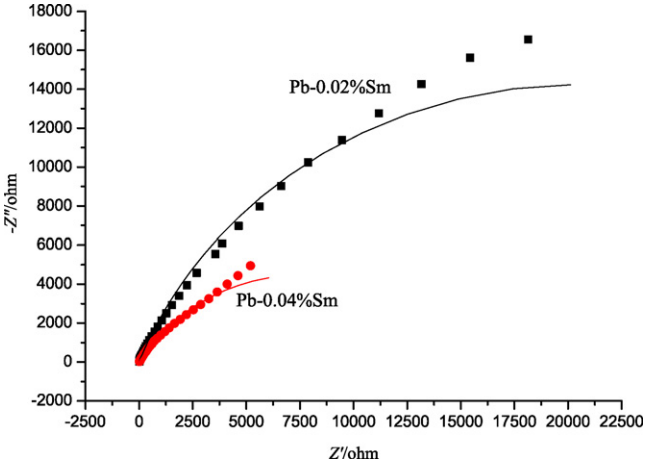

Fig. 6. Nyquist plot of impedance data of Pb–0.02%Sm electrode and Pb–0.04%Sm electrode, polarized at 0.9 V in 4.87 M H_2SO_4 for 1 h, frequency range from 10^5 to 10 Hz.

3: Pb–0.04%Sm, 4: Pb–0.12%Sm), as shown in Figs. 5 and 6. The electrochemical impedance plot of the pure-lead electrode is similar to that of the Pb–0.12%Sm electrode. The plots show a semicircular part at high frequency and a linear part at low frequency that are associated with an electron-transfer step and diffusion-controlled step, respectively. Consequently, the electrochemical behaviours shown in Fig. 5 can be represented by a simple equivalent circuit (Fig. 7). The fitting results for the Pb and Pb–0.12%Sm electrodes are listed in Table 3.

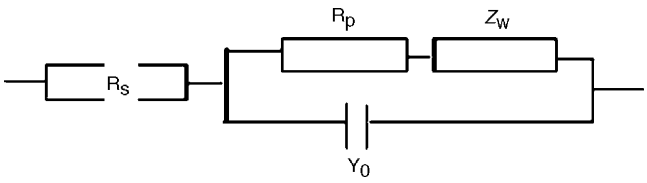

Fig. 7. Equivalent circuit used to fit impedance data measured during PbO growth on Pb electrode and Pb–0.12%Sm electrode.

Table 3
Example of fitting values computed using an equivalent circuit (Fig. 7) from EIS data recorded during oxidation of Pb and of Pb–0.12%Sm alloy at 0.9 V in 4.87 M H_2SO_4

	Pb		Pb–0.12%Sm	
R_s (Ω)	−0.369		0.156	
R_p (kΩ)	0.385	11[a]	0.274	8.057[a]
Y_o (F)	3.55E−08	1.83[a]	5.09E−08	1.372[a]
n	0.768	3.96[a]	0.786	2.267[a]
W (Ω)	1.54E−04	3.35[a]	3.73E−04	3.547[a]

[a] Est. error (%).

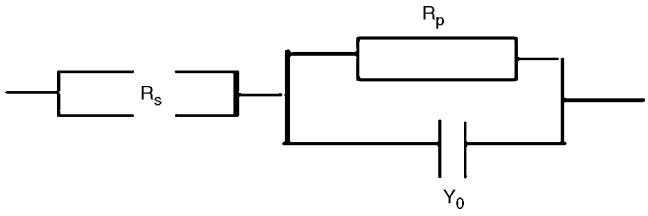

Fig. 8. Equivalent circuit used to fit impedance data measured during PbO growth on Pb–0.02%Sm electrode and Pb–0.04%Sm electrode.

The electrochemical impedance plot of the Pb–0.02%Sm electrode is analogous to that of the Pb–0.04%Sm electrode but only consists of a semicircular part that indicates an electron-transfer step. The equivalent circuit given in Fig. 8 represents the electrochemical impedance behaviour in Fig. 6. The fitting results for the two electrodes are presented in Table 4. As high as 14–18 Kr, the electrochemical impedances of the oxides on the Pb–0.02%Sm Pb–0.04%Sm electrodes are much more than those of the oxides on the Pb and Pb–0.12%Sm electrodes. It is concluded that the electrochemical impedance of oxide formed on the electrode surface is high when the alloy contains 0.02–0.04%Sm but is greatly reduced with 0.12%Sm.

3.1.4. LSV study

The potentials of the Pb and Pb–Sm electrodes were kept at 0.5, 0.9 or 1.1 V for 1 h and then swept in the negative direction to −1.2 V at a rate of 1 mV s^{-1} in 4.87 M H_2SO_4. Typical voltammograms for Pb electrode are shown in Figs. 9–11. As shown in Fig. 11, peak 3 corresponds to the reduction of PbO_2 to $PbSO_4$, peak 2 to the reduction of Pb(II) oxides to Pb, and peak 1 to the reduction of $PbSO_4$ to Pb. The voltammograms for Pb–Sm electrodes are not shown since they are similar as that of the Pb electrode. The reduction current of peaks 1, 2 and 3, $I_{Pb(II)/Pb}$ and $I_{PbSO_4/Pb}$ and $I_{PbO_2/PbSO_4}$, for Pb and

Table 4
Example of fitting values computed using an equivalent circuit (Fig. 8) from EIS data recorded during oxidation of Pb–0.02%Sm alloy and of Pb–0.04%Sm alloy at 0.9 V in 4.87 M H_2SO_4

	Pb–0.02%Sm		Pb–0.04%Sm	
R_s (Ω)	10	16.2[a]	−4.34	18.7[a]
R_p (kΩ)	41.1	7.5[a]	15.45	6.3[a]
Y_o (F)	1.73E−08	6.86[a]	1.48E−08	5.9[a]
n	0.77	0.76[a]	0.67	0.64[a]

[a] Est. error (%).

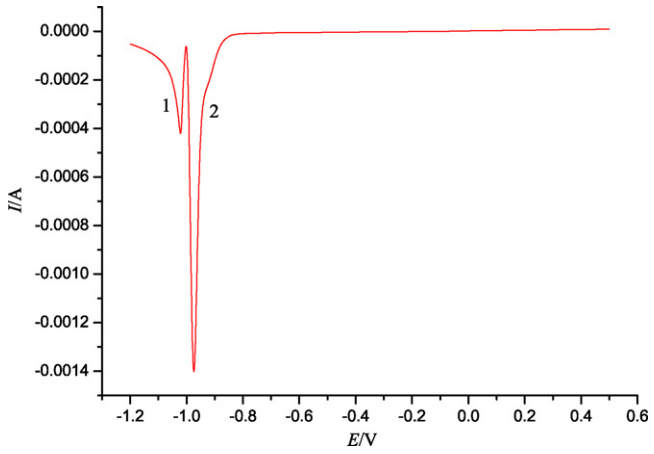

Fig. 9. Voltammograms for anodic films formed on Pb at 0.5 V for 1 h in H_2SO_4 (4.87 M L^{-1}), $v = 1$ mV s^{-1}.

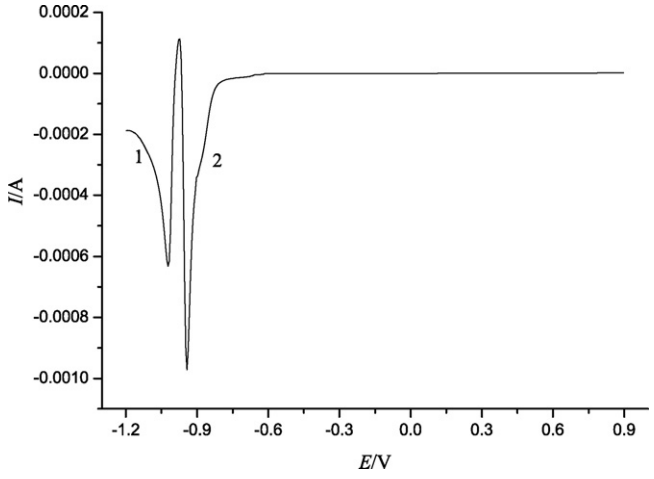

Fig. 10. Voltammograms for anodic films formed on Pb at 0.9 V for 1 h in H_2SO_4 (4.87 M L^{-1}), $v = 1$ mV s^{-1}.

Pb–Sm electrodes are listed in Table 7. The reduction potentials of peaks 1–3 for Pb are −0.98, −0.91 and 1.1 V, respectively, those for Pb–Sm electrodes are −0.97, −0.90 and 1.1 V, respectively.

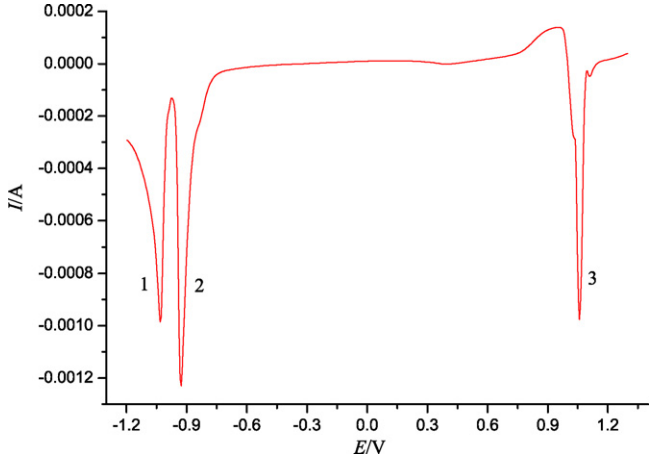

Fig. 11. Voltammograms for anodic films formed on Pb at 1.3 V for 1 h in H_2SO_4 (4.87 M), $v = 1$ mV s^{-1}.

Table 5
Peak current of voltammograms for anodic films formed on Pb and Pb–Sm alloy at 0.5 V

Electrode	E_1 (V)	I_1 (mA)	E_2 (V)	I_2 (mA)
Pb	−0.977	−0.42	−0.927	−1.4
Pb–0.02%Sm	−0.962	−0.592	−0.891	−0.692
Pb–0.04%Sm	−0.967	−0.456	−0.885	−0.964
Pb–0.12%Sm	−0.982	−0.299	−0.933	−1.07

Table 6
Peak current of voltammograms for anodic films formed on Pb and Pb–Sm alloy at 0.9 V

Electrode	E_1 (V)	I_1 (mA)	E_2 (V)	I_2 (mA)
Pb	−0.977	−0.5408	−0.907	−1.52
Pb–0.02%Sm	−0.9613	−0.793	−0.897	−1.33
Pb–0.04%Sm	−0.9639	−0.655	−0.895	−1.71
Pb–0.12%Sm	−0.977	−0.44	−0.887	−1.2

Table 7
Peak current of voltammograms for anodic films formed on Pb and Pb–Sm alloy at 1.3 V

Electrode	E_1 (V)	I_1 (mA)	E_2 (V)	I_2 (mA)	E_3 (V)	I_3 (mA)
Pb	−0.987	−0.985	−0.884	−1.23	1.103	−0.976
Pb–0.02%Sm	−0.965	−0.97	−0.859	−1.12	1.108	−0.862
Pb–0.04%Sm	−0.969	−1.303	−0.839	−1.034	1.106	−0.968
Pb–0.12%Sm	−0.987	−0.89	−0.877	−1.4	1.103	−0.74

It can been seen from the data in Tables 5–7 that the current of peak 1 for Pb–Sm electrode is lower than that for Pb, and the current of the peak 2 for Pb–Sm electrode is higher than that for Pb after 0.02 or 0.04% Sm is added. This suggests that adding 0.02 or 0.04% Sm can promote the growth of the $PbSO_4$ membrane but inhibits the growth of the anodic Pb(II) oxides film. On the other hand, adding 0.12% Sm can inhibit the growth of both the $PbSO_4$ membrane and the anodic Pb(II) oxides film.

3.1.5. Oxygen evolution

Water is decomposed to release oxygen at the end of charge and during overcharge of the lead dioxide plates in lead–acid batteries when a Pb/PbO_2 electrode is polarised in the PbO_2 potential region ($\varphi \geq 1.0$ V) [18–20]. Linear sweep voltammetry of Pb and Pb–Sm alloy electrodes in 4.87 M H_2SO_4 are shown in Fig. 12 and the kinetic parameters of oxygen evolution are listed in Table 8. As shown and in Fig. 13, a β-PbO_2 membrane is formed on the Pb and Pb–Sm electrodes from 1.45 to 1.60 V, and that the presence of samarium does not change the control step of the chemical reaction that occurs on the

Table 8
Kinetic parameters of oxygen evolution reaction on lead and lead–samarium obtained by LSV method

Electrode	E	b	R
Pb	1.83155	0.10736	0.9972
Pb–0.02%Sm	1.84055	0.11291	0.99633
Pb–0.04%Sm	1.83199	0.10678	0.99608
Pb–0.12%Sm	1.83258	0.10963	0.99691

Table 9
Hardness of test alloy

	1#	3#	4#	5#	6#	7#
Ageing hardness for 2 days (kgf mm^{-2})$^{-1}$	9	9.02	9.3	9.2	9.2	9.8
Ageing hardness for 8 days (kgf mm^{-2})$^{-1}$	9.25	9.5	9.9	9.4	10	10.7

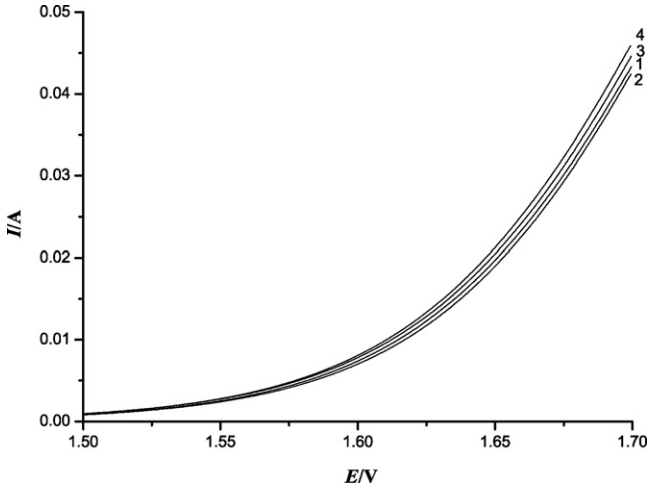

Fig. 12. LSV of Pb and Pb–Sm alloy electrode in 4.87 M H_2SO_4 solutions, scan rate 2 mV s^{-1}, electrodes: 1, Pb; 2, Pb–0.02%Sm; 3, Pb–0.04%Sm; 4, Pb–0.12%Sm.

electrode surface. From Table 8, it can be seen that the overpotential of oxygen evolution on the Pb–0.02%Sm, Pb–0.04%Sm and Pb–0.12%Sm electrodes is much higher than that on Pb electrode. Thus, preliminary results indicate that samarium can inhibit oxygen evolution in VRLA batteries.

The overpotential of oxygen evolution is highest on the Pb–0.02%Sm electrode. In other words oxygen evolution is least on this electrode and therefore the alloy is more suitable for use in VRLA batteries.

Nyquist plots of the oxygen evolution reaction on lead and lead–samarium alloy electrodes are given in Fig. 14. The plots for the four electrodes are similar at the same potential and

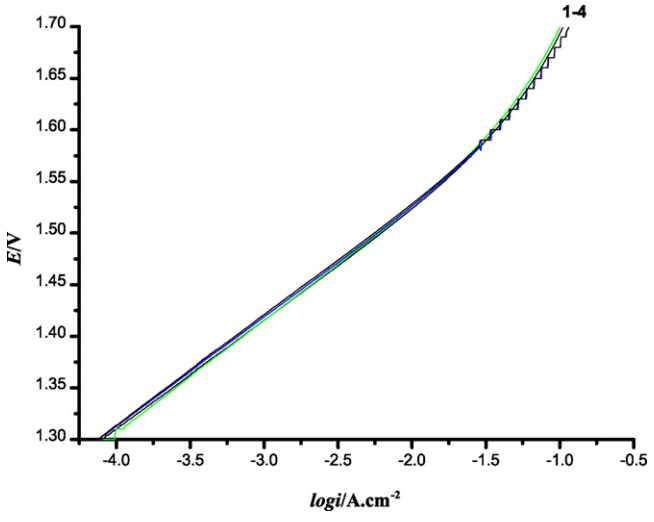

Fig. 13. Relationship between potential and logarithm of current.

exhibit a semicircular part at high frequency that indicates control by electron transfer. The semicircular radius of the plots for each of the Pb–0.02%Sm, Pb–0.04%Sm and Pb–0.12%Sm electrodes is much larger than that of the Pb electrode, that is, the oxygen evolution reaction resistance of the Pb–0.02%Sm, Pb–0.04%Sm and Pb–0.12%Sm electrodes are more than that of the Pb electrode. Consequently, it is found that samarium can inhibit the oxygen evolution, and adding 0.02% Sm exerts the best effect.

3.2. Pb–Ca–Sn–Al–Sm alloy

3.2.1. Hardness test

A grid alloy should have sufficient hardness and yield strength to suffer mechanical deformation during manufacture and service of the battery. The change in hardness during of testing of the alloys is shown in Table 9. The hardness of the Pb–0.085%Ca–0.6%Sn–0.005%Al–0.15%Sm alloy (#4) is the largest while that of the Pb–0.05%Ca–0.6%Sn–0.005%Al alloy (#1) is the smallest. Adding an amount of samarium can improve the hardness of lead–calcium alloys now used in factories, but has little influence on ageing hardness.

With a suitable atomic size, samarium is likely to sediment on the crystal boundary and phase boundary when the alloy is solidifying. Occupying the vacancy of the alloy, samarium atoms may slow the diffusion of other atoms in the alloy and there by hinder crystal growth. Therefore, a finer casting structure of alloy will be obtained. The finer the crystal, the more boundaries are obtained. Consequently, the largest deformation that the alloy can suffer is improved and this means that the hardness of alloy is enhanced.

3.2.2. SEM micrographs of corrosion layer surface

Scanning electron micrographs of the surface and the section plane of the corrosion layer formed on a Pb–Ca–Sn–Al–Sm substrate after potentiostatic polarization are shown in Figs. 15 and 16, respectively.

The surface of the corrosion layer (Fig. 15(a)) is flat and the grains of the corrosion product are compact, which may loosen the adhesion between the grid and the active material. With the addition of samarium, the surfaces of the corrosion layers on Pb–0.05%Ca–0.6%Sn–0.005%Al–0.01%Sm, Pb–0.05%Ca–0.6%Sn–0.005%Al–0.1%Sm, Pb–0.05%Ca–0.6%Sn–0.005%Al–0.15%Sm and Pb–0.08%Ca–0.6%Sn–0.005%Al–0.15%Sm alloys becomes so porous that active material can sit in the apertures to contact the grid surface intimately with the effective surface area of corrosion product.

The sections of the corrosion layer in Fig. 16 also indicate that the corrosion layer is too compact and thin to combine the active material.

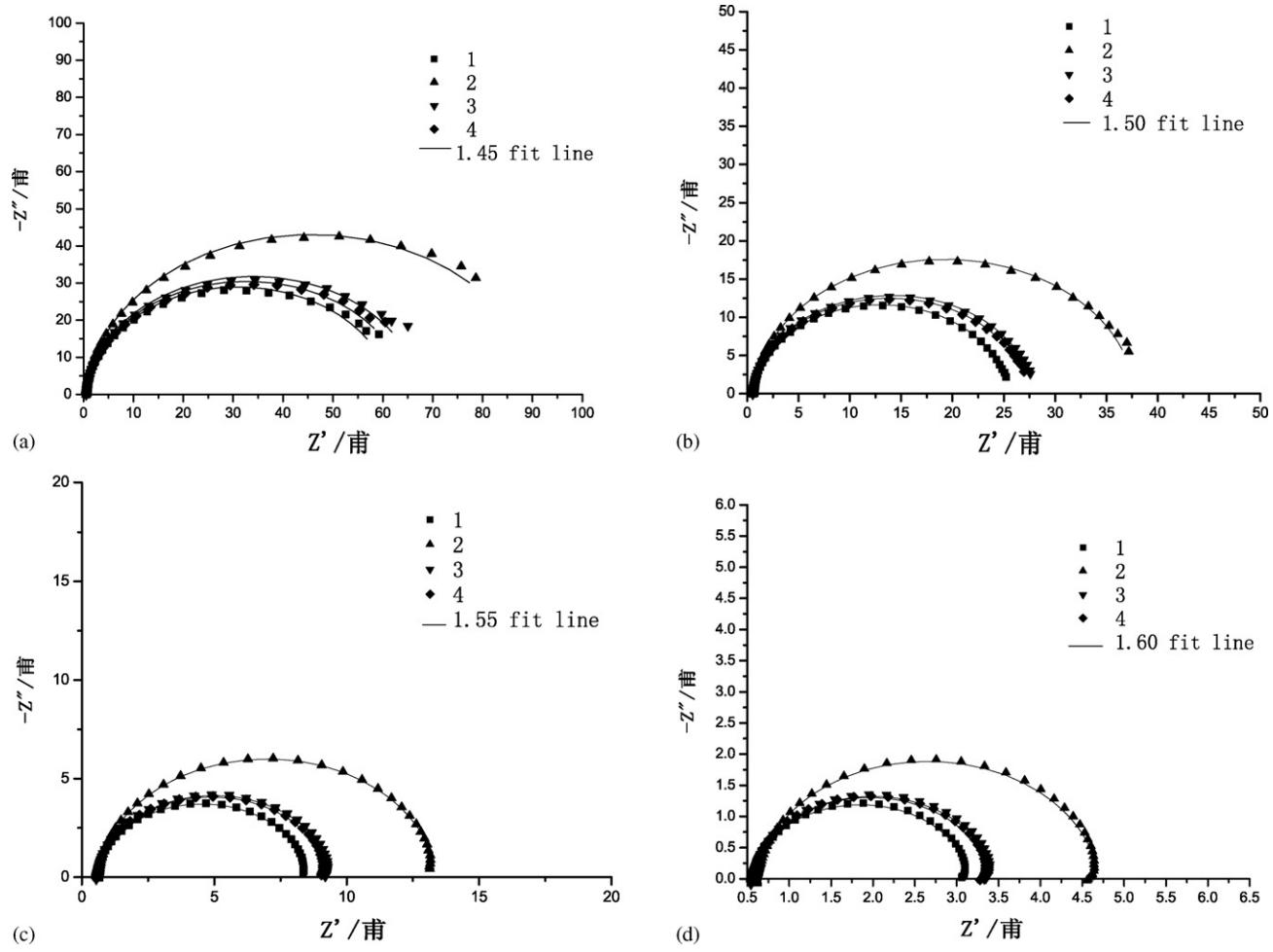

Fig. 14. Nyquist plots of oxygen evolution reaction on lead and lead–samarium alloy electrodes in 4.87 M H_2SO_4 solutions at different potentials ((a) 1.45 V; (b) 1.50 V; (c) 1.55 V; (d) 1.60 V), electrodes: 1, Pb; 2, Pb–0.02%Sm; 3, Pb–0.04%Sm; 4, Pb–0.12%Sm.

3.2.3. Cyclic votammetry

Cyclic voltammograms of Pb–0.05%Ca–0.6%Sn–0.005%Al and Pb–0.05%Ca–0.6%Sn–0.005%Al–0.01%Sm alloys are presented in Figs. 17 and 18. On the positive sweep, two anodic peaks (A_1 and A_3) can be observed; they correspond to the oxidation of Pb to $PbSO_4$, the formation of β-PbO_2 from $PbSO_4$, and the evolution of oxygen, respectively. On the negative sweep, one anodic peak (A_2) and four cathodic peaks (C_1, C_2, C_3 and C_4) are observed, where peak A_1 corresponds to the oxidation of Pb below the $PbSO_4$ membrane, peak C_1 to the reduction of PbO_2, peak C_2 to the reduction of PbO and PbO_n, peak C_3 to the reduction of $PbSO_4$ to Pb, and the peak C_4 to hydrogen evolution.

The reduction peak charge for Pb–Ca–Sn–Al and Pb–Ca–Sn–Al–Sm electrodes is listed in Table 10. With the addition of samarium, the charges of peaks A_1 and A_2 decrease sharply and the potentials of the peaks shift in a positive direction. This suggests that the oxidation of Pb to $PbSO_4$ and the oxidation of Pb to Pb(II) is hundered. On the negative sweep, the electric charges of peaks C_1 and C_2 also decrease, which indicates that samarium will inhibit the growth of $PbSO_4$ and PbO on Pb–Ca–Sn–Al alloy.

3.2.4. EIS study

When the potential of anodic oxidation for lead in sulfuric acid solution is in the PbO potential region (−0.40 to 0.95 V), an anodic film of complex composition is formed on the lead electrode. Typical Nyquist plots of the anodic films on Pb–Ca–Sn–Al and Pb–Ca–Sn–Al–Sm electrodes are depicted in Fig. 19. By comparing the values, it can be found that $-Z$ values of the film on Pb–Ca–Sn–Al–Sm electrodes differ significantly from that on the Pb–Ca–Sn–Al electrode.

3.2.5. Battery cycle-life test

Cycle-life tests of 12-V/10-Ah (2 h rate) VRLA batteries with Pb–Ca–Sn–Al alloy, Pb–Ca–Sn–Al–Sm alloy or Pb–Sb–Cd alloy for the positive grids were performed at 25 °C. The results are shown in Fig. 20. All the negative grids were made from Pb–Ca–Sn–Al. The cycle-life of electric bicycle batteries is tested according to Chinese machine industry standard 'VRLA Batteries Used for Electric Moped' (JB/T10262-2001). After charging at a constant potential 16 V and with a current 1.5 A for 5.6 h, a battery is discharged at a constant current of 5 A for 1.4 h. The test results are shown in Fig. 18 and demonstrate that the deep–cycle lives of batteries with Pb–Ca–Sn–Al–Sm posi-

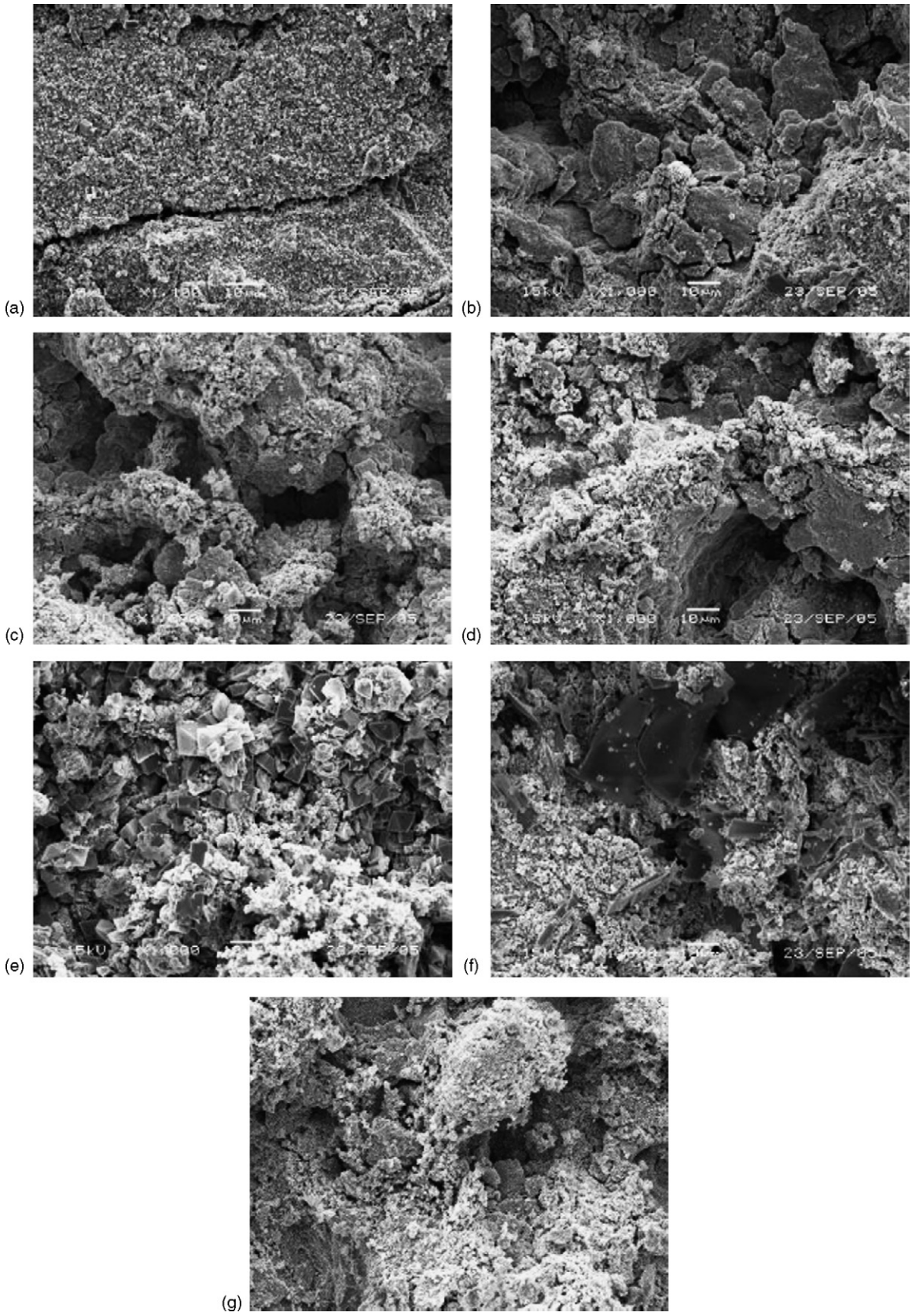

Fig. 15. SEM micrographs of surface of corrosion layer (a) Pb–0.05%Ca–0.6%Sn–0.005%Al; (b) Pb–0.05%Ca–0.6%Sn–0.005%Al–0.01%Sm; (c) Pb–0.05%Ca–0.6%Sn–0.005%Al–0.1%Sm; (d) Pb–0.05%Ca–0.6%Sn–0.005%Al–0.15%Sm; (e) Pb–0.05%Ca–0.6%Sn–0.005%Al–0.2%Sm; (f) Pb–0.05%Ca–0.6%Sn–0.005%Al–0.25%Sm; (g) Pb–0.085%Ca–0.6%Sn–0.005%Al–0.15%Sm.

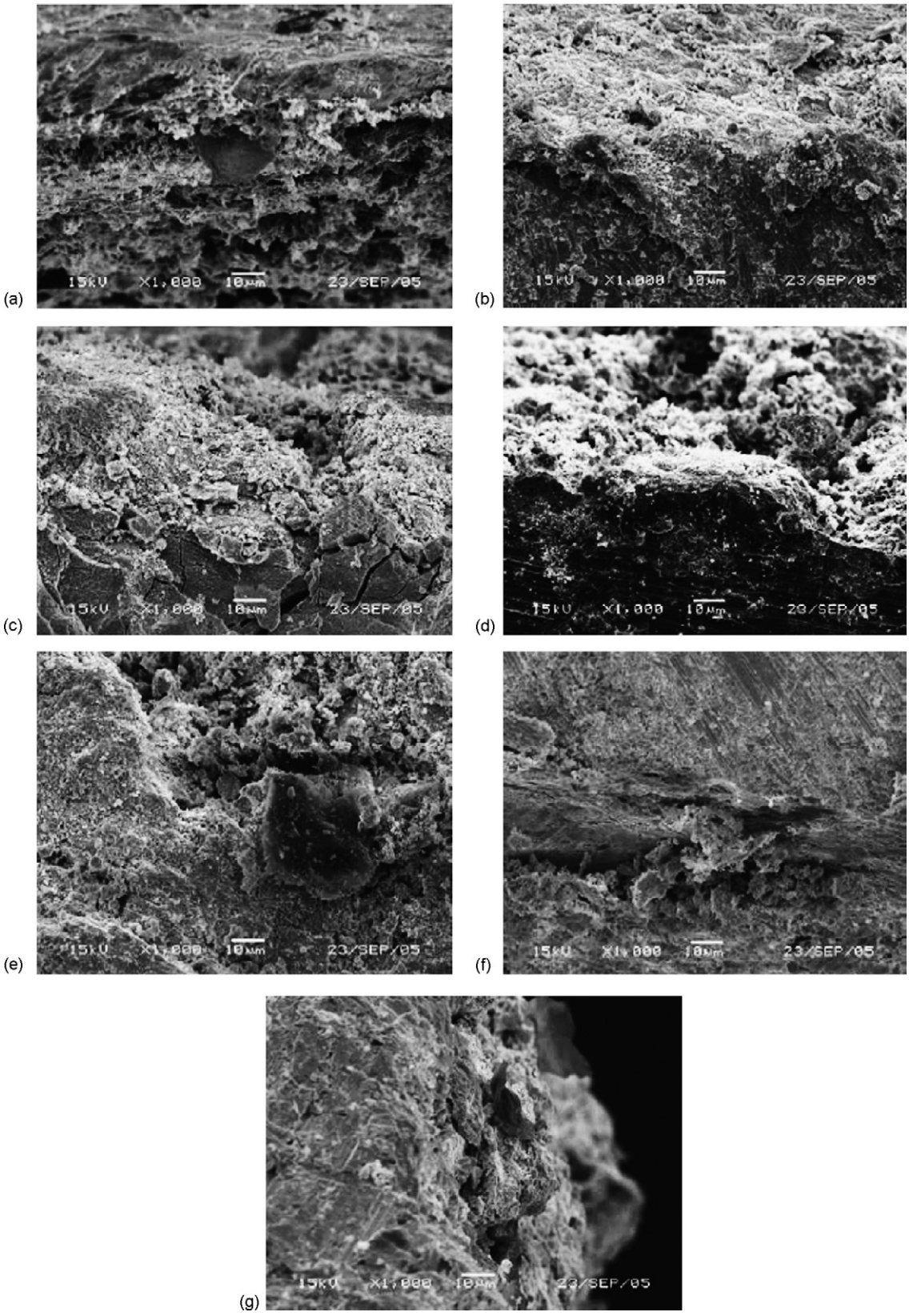

Fig. 16. SEM micrographs of section of corrosion layer (a) Pb–0.05%Ca–0.6%Sn–0.005%Al; (b) Pb–0.05%Ca–0.6%Sn–0.005%Al–0.01%Sm; (c) Pb–0.05%Ca–0.6%Sn–0.005%Al–0.1%Sm; (d) Pb–0.05%Ca–0.6%Sn–0.005%Al–0.15%Sm; (e) Pb–0.05%Ca–0.6%Sn–0.005%Al–0.2%Sm; (f) Pb–0.05%Ca–0.6%Sn–0.005%Al–0.25%Sm; (g) Pb–0.085%Ca–0.6%Sn–0.005%Al–0.15%Sm.

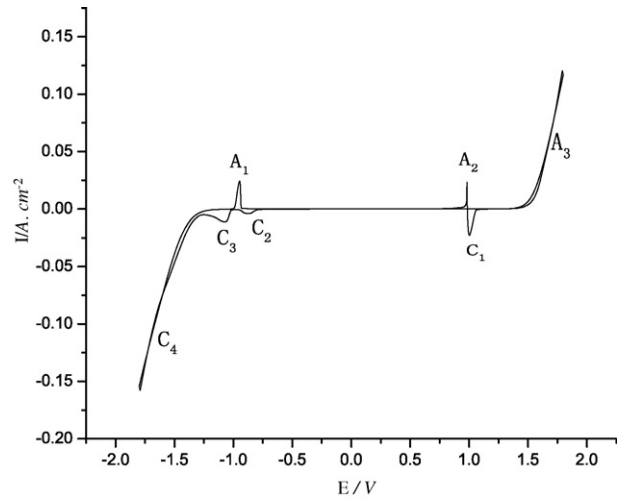

Fig. 17. Cyclic voltammograms at 75th cycle of Pb–Ca–Sn–Al electrode in 4.87 M H_2SO_4 solution ($v = 5\,mV\,s^{-1}$).

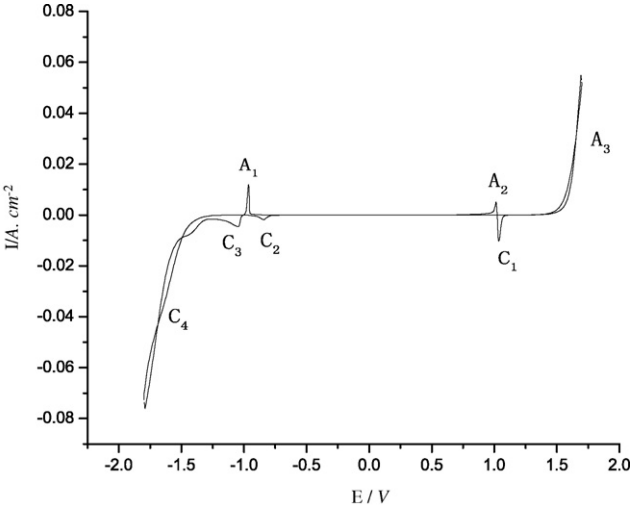

Fig. 18. Cyclic voltammograms at 75th cycle of Pb–Ca–Sn–Al–0.01%Sm electrode in 4.87 M H_2SO_4 solution ($v = 5\,mV\,s^{-1}$).

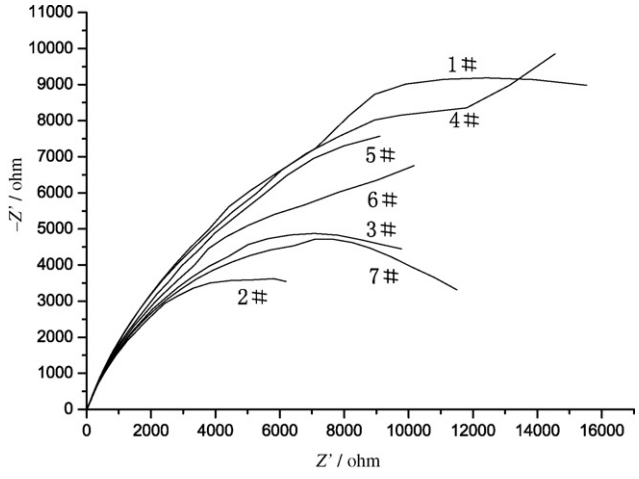

Fig. 19. Nyquist plots for anodic films formed on Pb–Ca–Sn–Al (1#) and Pb–Ca–Sn–Al–Sm (2#–7#) electrodes at 0.9 V in H_2SO_4 (4.87 M) for 1 h at 25 °C.

Table 10
Peak potential and peak current of LSV for Pb–Ca–Sn–Al and Pb–Ca–Sn–Al–Sm alloys

	1#	2#	3#	4#	5#	6#	7#
A_1							
E (V)	−0.946	−0.964	−0.96	−0.97	−0.968	−0.966	−0.976
Q (C cm^{-2})	1.582	0.472	0.302	0.596	0.521	0.655	0.638
A_2							
E (V)	0.982	1.014	1.014	1.004	1.012	1	1.008
Q (C cm^{-2})	0.649	0.347	0.291	0.257	0.358	0.193	0.208
A_3							
E (V)	1.792	1.8	1.8	1.786	1.8	1.792	1.778
Q (C cm^{-2})	11.56	6.446	4.099	6.924	6.805	9.133	8.357
C_1							
E (V)	1.002	1.036	1.038	1.034	1.036	1.034	1.04
Q (C cm^{-2})	1.966	0.508	0.273	0.879	0.578	1.109	1.038
C_2							
E (V)	−0.868	−0.842	−0.842	−0.862	−0.846	−0.898	−0.864
Q (C cm^{-2})	0.839	0.275	0.195	0.42	0.35	0.521	0.415
C_3							
E (V)	−1.07	−1.046	−1.05	−1.046	−1.05	−1.046	−1.038
Q (C cm^{-2})	3.502	1.387	0.955	1.265	1.46	1.474	1.572
C_4							
E (V)	−1.7	−1.7	−1.7	−1.7	−1.7	−1.7	−1.7
Q (C cm^{-2})	39.375	11.043	6.844	54.536	10.684	78.51	8.357

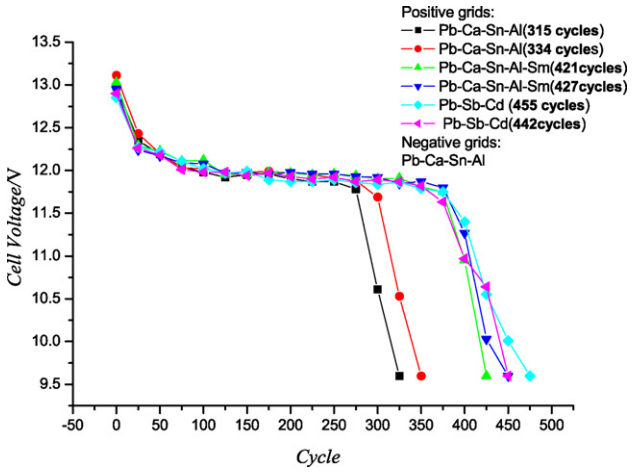

Fig. 20. Deep cycle-life (70% DoD, 2 h rate) of electric bicycle VRLA batteries.

tive grids are longer than that of a battery with Pb–Ca–Sn–Al positive grids, but are close to that of a battery with Pb–Cd–Sb grids.

4. Conclusions

(1) According to the calculation of d value from the XRD patterns of lead and lead–samarium binary alloys, it is possible to conclude that finer grains are obtained with the addition of samarium.
(2) The self-depassivation behaviour of Pb and of Pb–0.12%Sm electrodes is similar, while that of Pb–0.02%Sm and Pb–0.04%Sm electrodes are similar when all the electrodes

are polarized at 0.9 or 1.1 V. The self-depassivation characteristics of Pb–Sm alloy electrodes that are first polarized at 1.3 V are similar to those for polarization at 0.9 or 1.1 V, but the self-depassivation curve of the Pb electrode arrives at the equilibrium potential of $PbSO_4$/Pb.

(3) Linearsweep voltammetry demonstrate that the addition of 0.02 and 0.04% Sm can promote the growth of the $PbSO_4$ membrane but inhibits that of the anodic Pb(II) oxides film. Adding 0.12% Sm, however, can inhibit both the growth of the $PbSO_4$ membrane and that of anodic Pb(II) oxides film.
(4) EIS studies show that the electrochemical impedance of the oxide formed on the electrode surface is high when the alloy contains 0.02 and 0.04% Sm, but is greatly reduced with 0.12%Sm.
(5) Samarium can inhibit the oxygen evolution, and adding 0.02% Sm causes a more effective inhibition compared with 0.04 or 0.12% Sm.
(6) Adding samarium can improve the hardness of the lead–calcium alloys that are widely used in factories in China. On the other hand, samarium has little influence on ageing hardness.
(7) Samarium will inhibit the growth of $PbSO_4$ and PbO on a Pb–Ca–Sn–Al alloy, and reduce the resistance of the $PbSO_4$ and PbO membranes.
(8) The cycle-life of electric bicycle VRLA batteries with Pb–Ca–Sn–Al–Sm positive grids is greater than that of batteries with Pb–Ca–Sn–Al positive grids, and is close to that of batteries with Pb–Sb–Cd positive grids.

References

[1] R. David Prengaman, J. Power Sources 53 (1994) 207.
[2] G.J. May, J. Power Sources 59 (1996) 147.
[3] R. David Prengaman, J. Power Sources 95 (2001) 224.
[4] D.W.H. Lambert, J.E. Manders, R.F. Nelson, K. Peters, D.A.J. Rand, M. Stevenson, J. Power Sources 88 (2000) 130.
[5] N. Bui, P. Mattesco, P. Simon, N. Pebere, J. Power Sources 73 (1998) 30.
[6] E. Rocca, J. Steinmetz, Electrochim. Acta 44 (1999) 4611.
[7] J. Hertz, C. Forniaseri, J.P. Hilger, M. Notin, J. Power Sources 46 (1993) 199.
[8] E. Rocca, Ph.D. Thesis, Nancy, France, 1999.
[9] J. Wei, L. Zhao, F.L. Sun, H. Yang, D.W. Chu, Chin. J. Nonferrous Met. 13 (2) (2003) 487.
[10] Y.B. Zhou, C.X. Yang, M. Ma, W.F. Zhou, H.T. Liu, Chem. J. Chin. Universities 24 (2003) 1677.
[11] Y.B. Zhou, C.X. Yang, W.F. Zhou, H.T. Liu, J. Alloys Compd. 365 (2004) 108.
[12] H.T. Liu, C.X. Yang, X.H. Zhang, Y.B. Zhou, W.F. Zhou, Chin. J. Chem. 20 (2002) 591.
[13] H.T. Liu, C.X. Yang, H.H. Liang, J. Yang, W.F. Zhou, Electrochemistry 7 (4) (2001) 439.
[14] H.T. Liu, J. Yang, H.H. Liang, J.H. Zhuang, W.F. Zhou, Electrochemistry 6 (3) (2000) 265.
[15] H.T. Liu, X.H. Zhang, J. Yang, C.X. Yang, W.F. Zhou, Acta Chim. Sin. 600 (4) (2002) 643.
[16] P. Ruetschi, R.T. Angstadt, J. Electrochem. Soc. 111 (12) (1964) 1323.
[17] P. Ruetschi, J. Electrochem. Soc. 120 (3) (1973) 331.
[18] D. Pavlov, B. Monahov, J. Electrochem. Soc. 143 (11) (1996) 3616.
[19] D. Pavlov, B. Monahov, J. Electrochem. Soc. 145 (1) (1998) 70.
[20] B. Monahov, D. Pavlov, D. Petrov, J. Power Sources 85 (2000) 59.